In Silico Assessment of Arrhythmic Risk in Infarcted Ventricles Engrafted with Engineered Heart Tissues

Ricardo M Rosales[1,2], Konstantinos A Mountris[3], Manuel Doblaré[1,2], Manuel M Mazo[4,5], Esther Pueyo[1,2]

[1] Aragon Institute of Engineering Research, University of Zaragoza, IIS Aragon, Zaragoza, Spain
[2] CIBER in Bioengineering, Biomaterials & Nanomedicine (CIBER-BBN), Spain
[3] Department of Mechanical Engineering, University College London, London, United Kingdom
[4] Regenerative Medicine Program, CIMA Universidad de Navarra, Pamplona, Spain
[5] Hematology and Cell Therapy, Clínica Universidad de Navarra, Pamplona, Spain

Abstract

Engineered heart tissues (EHTs) from human induced pluripotent stem cell-derived cardiomyocytes (hiPSC-CMs) represent novel alternatives to repair damaged cardiac tissue after myocardial infarction (MI). However, their associated slow conduction and prolonged action potential duration (APD) can favor proarrhythmicity.

We coupled biventricular (BiV) and EHT in silico electrophysiological models. The BiV model, defined from magnetic resonance imaging, included an MI region. The EHT model was deformed to follow the epicardial surface. Different values of EHT electrical conductivity (EHTc) and degree of myocardial attachment (EHTa) were tested.

Results showed that even a minimum degree of EHTa inhibited EHT automaticity. Activation time and APD were driven by myocardial tissue when engrafted. Importantly, higher EHTc and EHTa led to lower repolarization gradients (RTGs), considered as a surrogate of arrhythmic risk. Maximum RTG decreased by 52.3 ms/mm when EHTa varied from 25 % to 100 % under low EHTc and decreased by 98.8 ms/mm when EHTc raised to 90 % of the myocardium conductivity under low EHTa.

Proarrhythmicity in cardiac tissue engineering highly depends on EHT conductivity and degree of engraftment on the myocardium.

1. Introduction

Tissue engineering techniques have been proposed to heal damaged cardiac tissue. In particular, remuscularization with human induced pluripotent stem cell-derived cardiomyocytes (hiPSC-CMs) has been suggested as a promising approach to restore cardiac pumping function after myocardial infarction (MI) [1].

Bio-printed scaffolds favor hiPSC-CMs maturation and improve cell organization and mechanical function of engineered heart tissues (EHTs) [2], but are still unable to mimic adult-like electrophysiological characteristics such as cell-to-cell connectivity and anisotropic cell alignment. Besides, EHT transplantation is a complex surgical procedure. Incomplete EHT engraftment on the myocardium frequently occurs due to formation of air bubbles, poor gluing or stitching, the need to control for cardiac relaxation-contraction cycles and the presence of fibrosis [1, 3].

Slow conductivity and prolonged action potential (AP) duration (APD), like those found in immature and poorly on-myocardium engrafted EHTs, increase proarrhythmic risk [4, 5]. To avoid expensive and time consuming experimental and clinical risk assessment studies, computational simulation studies using biophysically detailed cellular AP models and realistic biventricular (BiV) geometries have been published recently [3, 5–7].

We present an *in silico* electrophysiological investigation in which we assess post-MI remuscularization with EHTs in terms of activation, repolarization and arrhythmic risk. The impact of concomitantly varying the EHT electrical conductivity (EHTc) and the degree of attachment on the myocardium (EHTa) is quantified and conclusions on the suitability for cardiac tissue engineering are drawn.

2. Materials and methods

2.1. Generation of *in silico* models

BiV segmentation was performed from a late-gadolinium enhanced magnetic resonance image (LGE-MRI), as illustrated in Figure 1a. The segmentation was discretized using a mean tetrahedral edge length of $800\,\mu\mathrm{m}$. Affected (AZ) and healthy (HZ) zones were defined in the segmented ventricles based on the high and low intensity of the voxels, respectively. The AZ was divided into bor-

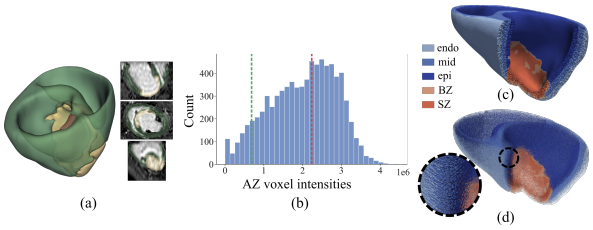

Figure 1: (a) LGE-MRI segmentation: healthy (green), affected (yellow) and remote healthy (brown) regions. (b) Histogram of AZ intensities, with thresholds S_{bz-}(green) and S_{bz+} (red). BiV tissue types (c) and fiber field (d).

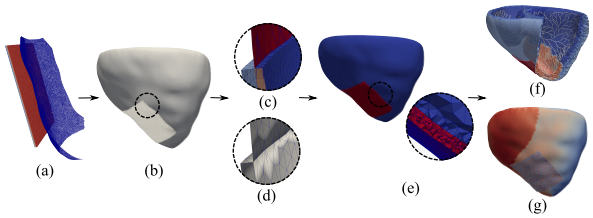

Figure 2: BiV-EHT model generation pipeline. (a) EHT and epicardial meshes (contact nodes in red). (b) Contacting BiV and EHT meshes. (c) Integrated BiV-EHT mesh with distinct regions and irregular triangles. (d) Cleaned BiV-EHT mesh. (e) Tetrahedral mesh with BiV (blue) and EHT (red) zones. BiV-EHT regions (f) and fiber field (g).

der (BZ) and scar (SZ) zones according to the full-width half-maximum method described in [8]. Specifically, two thresholds were defined as shown in Figure 1b, with S_{bz+} corresponding to $50\,\%$ of the AZ maximum signal intensity and S_{bz-} to the maximum signal intensity in a remote HZ. SZ was selected as the part of AZ whose signal intensity was above S_{bz+} and BZ as the part of AZ whose signal intensity lied in $[S_{bz-}, S_{bz+}]$. The obtained BZ and SZ were interpolated to the BiV mesh using radial basis functions. A rule-based fiber field was computed as in [9].

Next, we proposed a pipeline, depicted in Figure 2, to define EHT models and couple them to the BiV model. A 4x4x1 mm^3 squared superficial mesh was generated for the EHT. A rigid transformation was used to bring the EHT closer to the MI region of the BiV mesh (Figure 2a). EHT contact nodes were defined as those in the face closest to the epicardial surface. Displacement vectors were computed from the differences between the positions of the EHT contact nodes and the nearest epicardial nodes. EHT imposed deformations based on this node-wise contact displacement resulted in an EHT deformation that followed the epicardial BiV surface (Figure 2b). Subsequently, approximately half of the EHT thickness was embedded into the BiV model and merged with it using an *XOR* operation between both triangular meshes. Irregular triangles leading to bad quality tetrahedralizations were cleaned with an isotropic explicit remeshing [10] of the BiV-EHT interface. The EHT part located inside the heart (blue region in Figure 2c) was deleted. The BiV-EHT mesh was discretized with maximum tetrahedral volumes of $1\,\mathrm{mm}^3$ for the BiV and $1\,\mu\mathrm{m}^3$ for the EHT, respectively, producing in total $2\,077\,367$ tetrahedrons and $349\,322$ nodes. Ventricular region definitions and fiber orientations were interpolated from the initial BiV model (Figure 2f and 2g). Random cell orientation was assigned to the EHT.

2.2. Electrophysiological simulations

The BiV endocardial conduction system (CS) and the transmural heterogeneity in HZ were defined as in [11]. Tissue electrical propagation was computed by numerically integrating the monodomain model with the in-house developed software *ELECTRA* [12]. Ventricular, hiPSC-CM and CS cellular APs were described by the O'Hara et al. ventricular myocyte model [13], the Paci et al. ventricular-like hiPSC-CM model [14] and the Stewart et al. Purkinje cell model [15], respectively. The BZ cellular AP model was defined by modulating some of the ionic current conductances in the O'Hara et al. model, as described in [16], in such a way that the APD was increased and the maximum AP amplitude was decreased. Cellular models were paced to steady-state by running 1000-second simulations. Each organ level simulation consisted of three cardiac cycles at $1\,\mathrm{Hz}$ pacing, with the last cycle being used for analysis. Stimuli of $80\,\mathrm{mA}$-magnitude and $1\,\mathrm{ms}$-duration were applied at the atrioventricular node. CS-activated ventricular nodes were located at a maximum distance of $1\,\mathrm{mm}$ from CS endpoints.

Orthotropic conductivity with transverse isotropy was considered. HZ and BZ longitudinal diffusivities were set to 0.0013 and $0.00095\ \mathrm{cm}^2/\mathrm{ms}$ (equivalent to 0.13 and $0.095\ \mathrm{S/m}$ for a membrane surface-to-volume ratio of $1000\,\mathrm{cm}^{-1}$ and capacitance per unit area of $1\,\mu\mathrm{F}/\mathrm{cm}^2$), respectively. The CS longitudinal diffusivity was set to $0.01\,\mathrm{cm}^2/\mathrm{ms}$ ($1\,\mathrm{S/m}$) and reduced near the CS endpoints to match ventricular diffusion as in [11]. The SZ was defined as non-conductive. Transverse-to-longitudinal diffusion ratios were set to 0.25 for HZ and EHT and to 0.32 for BZ, similarly to previous studies modeling healthy cardiac conduction anisotropy and post-MI alterations [11, 16].

2.3. EHT conductivity and engraftment

EHTc values equivalent to $10\,\%$, $50\,\%$ and $90\,\%$ of that in healthy tissue were tested. Discontinuous meshes were created by duplicating the mesh nodes and edges in the BiV-EHT interface to model $0\,\%$, $25\,\%$, $50\,\%$ and $75\,\%$ of EHTa, as can be seen in Figure 3. The initially defined contiguous BiV-EHT mesh represented $100\,\%$ EHT engraft-

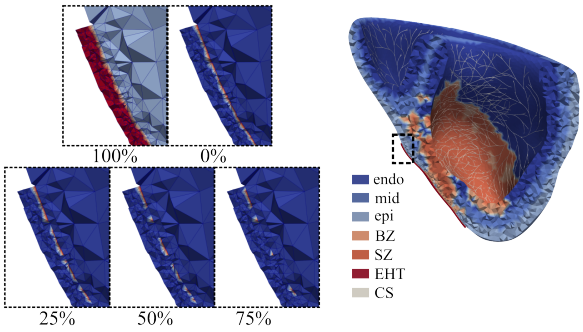

Figure 3: BiV-EHT model for different EHTa values. Unattached regions are shown in red.

ment. Non-engrafted regions were set as non-conductive by blocking the sodium current, I_{Na}, and by setting the longitudinal diffusivity to zero.

We evaluated the EHT activation time (AT), APD at $90\,\%$ repolarization (APD_{90}), conduction velocity (CV) and repolarization time gradients (RTGs) from the numerically integrated transmembrane voltage. Briefly, AT was computed as the time elapsed from a fixed time reference to the time when the AP upstroke crossed $0\,\mathrm{mV}$. APD_{90} was calculated as the time difference between the time points of maximum voltage derivative in the AP upstroke and when $90\,\%$ repolarization from AP peak to diastolic membrane potential was reached. The repolarization time (RT) was measured by summing AT and APD_{90}. To compute the spatial (RTG) or temporal (CV) gradients nodewisely, the vector v_{ab} between two nodes n_a and n_b was defined. In the case of RTG, v_{ab} magnitude was equal to the ratio of the difference between n_a and n_b RTs and their Euclidean distance. For CV, v_{ab} was equal to the ratio of the Euclidean distance between n_a and n_b and their AT difference. Next, the mean gradient vector between a central node and its neighbouring nodes within a radius of $500\,\mu\mathrm{m}$ was calculated, with the radius value chosen to approximately cover the EHT thickness.

3. Results and discussion

Figure 4 shows the statistical distributions of AT, APD_{90} and RTG calculated over the EHT. As can be observed, if the EHT was fully unattached to the myocardium, the hiPSC-CMs retained their automaticity and high AT values were measured. In this case, the higher the EHTc, the more delayed the AT in absolute terms and the faster the CV within the EHT. With only minimum EHTa, a large decrement in AT and loss of automaticity in the EHT could be observed. As an example, for $10\,\%$ EHTc, the entire EHT depolarization took $262\,\mathrm{ms}$ when the EHT was fully unattached, while it took around $140\,\mathrm{ms}$ when the EHT was engrafted even if minimally. For variations in EHTa

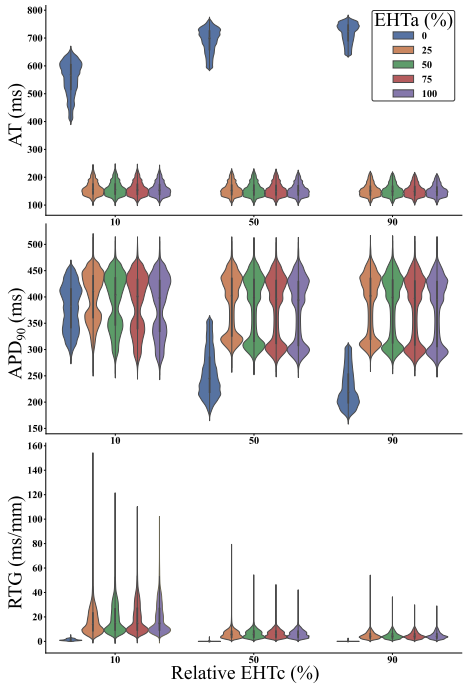

Figure 4: AT, APD_{90} and RTG versus EHTc and EHTa.

from $25\,\%$ to $100\,\%$, AT barely changed. Thus, with any level of attachment, even if low, the EHT depolarization seemed to be driven by the host myocardium, as EHTc-related AT variability practically vanished, in agreement with previous studies [3,5]. CV at the EHT was practically unchanged when varying EHTa, whereas higher EHTc increased the CV. Mean CVs of 7.8, 20.4 and $25.8\,\mathrm{cm/s}$ were measured for $10\,\%$, $50\,\%$ and $90\,\%$ EHTc.

For $0\,\%$ EHTa, median APD_{90} was reduced from 383 to $219\,\mathrm{ms}$ for $10\,\%$ and $90\,\%$ EHTc, respectively. Thus, higher EHTc accelerated hiPSC-CMs repolarization due to a source-sink mismatch leading to more adult-like APD_{90}. Also, APD_{90} slightly reduced with increasing EHTa. Median values of 402, 399, 396 and $394\,\mathrm{ms}$ were computed when EHTa was $25\,\%$, $50\,\%$, $75\,\%$ and $100\,\%$, respectively. In this study, EHT mostly covered BZ and not HZ. Thus, APD_{90} reduction with EHTc when the EHT was unattached was attenuated for minimal EHTa, possibly due to the higher BZ-to-EHT exerted electrotonic load. On the other hand, EHT APD_{90} reduction with increasing EHTa could be due to a higher HZ-to-EHT electrotonic load, which drags APD_{90} in the EHT to lower values, as observed in [6, 17].

As expected, RTG was almost null for fully unattached EHT. Median RTGs were similar for all EHTa values, as RTG was measured in the whole EHT. For the minimum EHTa of $25\,\%$, the maximum RTG was decreased by $98.8\,\mathrm{ms/mm}$ when EHTc increased from $10\,\%$ to $90\,\%$.

Thus, arrhythmic risk attenuation was found for high EHTc in association with smooth electrophysiological integration. Further arrhythmic risk reduction was found for high EHTa, as maximum RTG was reduced by as much as $52.3\,\mathrm{ms/mm}$ from minimum to complete EHTa when the minimum $10\,\%$ EHTc was set. Maximum RTGs, even for the highest EHTc and EHTa ($28.5\,\mathrm{ms/mm}$), were remarkably above the RTG thresholds experimentally reported to lead to unidirectional blocks ($3.2\,\mathrm{ms/mm}$) [4]. Thus, biomimetic EHTc and high EHTa seem vital to lower arrhythmic vulnerability.

4. Conclusion

Increased EHT electrical conductivity and degree of engraftment on the myocardium decrease proarrhythmic risk in cardiac tissue engineering.

Acknowledgments

This work was supported by EU H2020 Program under G.A. 874827 (BRAV3), by Ministerio de Ciencia e Innovación (Spain) through projects PID2019-105674RB-I00, PID2022-140556OB-I00 and TED2021-130459B-I00, by European Social Fund (EU) and Aragón Government through project LMP94_21 and BSICoS group T39_23R.

References

[1] Leor J, Amsalem Y, Cohen S. Cells, Scaffolds, and Molecules for Myocardial Tissue Engineering. Pharmacology Therapeutics 2005;105(2):151–163.

[2] Kristen M, Ainsworth MJ, Chirico N, Ven CFTvd, Doevendans PA, Sluijter JPG, Malda J, Mil Av, Castilho M. Fiber Scaffold Patterning for Mending Hearts: 3D Organization Bringing the Next Step. Advanced Healthcare Materials 2020;9(1):1900775.

[3] Yu JK, Liang JA, Franceschi WH, Huang Q, Pashakhanloo F, Sung E, Boyle PM, Trayanova NA. Assessment of Arrhythmia Mechanism and Burden of the Infarcted Ventricles Following Remuscularization With Pluripotent Stem Cell-Derived Cardiomyocyte Patches Using Patient-Derived Models. Cardiovascular Research 2022;118(5):1247–1261.

[4] Laurita KR, Rosenbaum DS. Interdependence of Modulated Dispersion and Tissue Structure in the Mechanism of Unidirectional Block. Circulation Research 2000; 87(10):922–928.

[5] Fassina D, M. Costa C, Bishop M, Plank G, Whitaker J, Harding SE, Niederer SA. Assessing the Arrhythmogenic Risk of Engineered Heart Tissue Patches Through In Silico Application on Infarcted Ventricle Models. Computers in Biology and Medicine 2023;154:106550.

[6] Fassina D, Costa CM, Longobardi S, Karabelas E, Plank G, Harding SE, Niederer SA. Modelling the Interaction Between Stem Cells Derived Cardiomyocytes Patches and Host Myocardium to Aid Non-Arrhythmic Engineered Heart Tissue Design. PLoS Comput Biol 2022; 18(4):e1010030.

[7] Gibbs CE, Marchianó S, Zhang K, Yang X, Murry CE, Boyle PM. Graft-Host Coupling Changes Can Lead to Engraftment Arrhythmia: A Computational Study. The Journal of Physiology 2023;JP284244.

[8] Schmidt A, et al. Infarct Tissue Heterogeneity by Magnetic Resonance Imaging Identifies Enhanced Cardiac Arrhythmia Susceptibility in Patients With Left Ventricular Dysfunction. Circulation 2007;115(15):2006–2014.

[9] Bayer JD, Blake RC, Plank G, Trayanova NA. A Novel Rule-Based Algorithm for Assigning Myocardial Fiber Orientation to Computational Heart Models. Ann Biomed Eng 2012;40(10):2243–2254.

[10] Cignoni P, Callieri M, Corsini M, Dellepiane M, Ganovelli F, Ranzuglia G. MeshLab: an Open-Source Mesh Processing Tool. In Scarano V, Chiara RD, Erra U (eds.), Eurographics Italian Chapter Conference. The Eurographics Association, 2008; .

[11] Rosales RM, Mountris KA, Doblaré M, Mazo MM, Pueyo E. Ventricular Conduction System Modeling for Electrophysiological Simulation of the Porcine Heart. 2022 Computing in Cardiology 2022;49:1–4.

[12] Mountris KA, Pueyo E. A Dual Adaptive Explicit Time Integration Algorithm for Efficiently Solving the Cardiac Monodomain Equation. Int J Numer Method Biomed Eng 2021;37(7):e3461.

[13] O'Hara T, Virág L, Varró A, Rudy Y. Simulation of the Undiseased Human Cardiac Ventricular Action Potential: Model Formulation and Experimental Validation. PLoS Comput Biol 2011;7(5):e1002061.

[14] Paci M, Hyttinen J, Aalto-Setälä K, Severi S. Computational Models of Ventricular- and Atrial-Like Human Induced Pluripotent Stem Cell Derived Cardiomyocytes. Annals of Biomedical Engineering 2013;41(11):2334–2348.

[15] Stewart P, Aslanidi OV, Noble D, Noble PJ, Boyett MR, Zhang H. Mathematical Models of the Electrical Action Potential of Purkinje Fibre Cells. Phil Trans R Soc A 2009; 367(1896):2225–2255.

[16] Lopez-Perez A, Sebastian R, Izquierdo M, Ruiz R, Bishop M, Ferrero JM. Personalized Cardiac Computational Models: From Clinical Data to Simulation of Infarct-Related Ventricular Tachycardia. Front Physiol 2019;10:580.

[17] Zaniboni M, Pollard AE, Yang L, Spitzer KW. Beat-To-Beat Repolarization Variability in Ventricular Myocytes and Its Suppression by Electrical Coupling. American Journal of Physiology Heart and Circulatory Physiology 2000; 278(3):H677–H687.

Address for correspondence:

Ricardo M. Rosales
University of Zaragoza, Campus Río Ebro, I+D Building, D-5.01.1B, Mariano Esquillor, s/n street, 50018, Zaragoza, Spain
rrosales@unizar.es